ACCSCIENCE PUBLISHING

International Journal of Bioprinting

RESEARCH ARTICLE

# Development and assessment of dimethyl sulfoxide-free antifreeze gelatin methacryloyl hydrogels for integrated three-dimensional bioprinting and cryopreservation

**Xin Li[1,2,3,4], Yukun Cao[2,3,4], Chengyuan Li[1], Chenxi Liu[2], Jia Tan[2,5], Xinli Zhou[2,3,4]* Yang Yu[6]*, and Xi Xia[1]***

[1]Department of Reproductive Medicine, Peking University Shenzhen Hospital, Shenzhen Peking University_the Hong Kong University of Science and Technology Medical Center, Shenzhen, Guangdong, China

[2]Department of Biomedical Engineering, University of Shanghai for Science and Technology, Shanghai, China

[3]Tumor Energy Therapy Laboratory, Shanghai Co-innovation Center for Energy Therapy of Tumors, Shanghai, China

[4]Cryobiology Laboratory, Shanghai Technical Service Platform for Cryopreservation of Biological Resources, Shanghai, China

[5]Key Laboratory for Tissue Engineering of Jiangxi Province, School of Medical Information Engineering, Gannan Medical University, Ganzhou, Jiangxi, China

[6]Department of Obstetrics and Gynecology, Peking University Third Hospital, Beijing, China

***Corresponding authors:**
Xinli Zhou
(zhouxinli@usst.edu.cn)
Yang Yu
(yuyang5012@hotmail.com)
Xi Xia
(xixia1126@hotmail.com)

**Citation:** Li X, Cao Y, Li C, et al. Development and assessment of dimethyl sulfoxide-free antifreeze gelatin methacryloyl hydrogels for integrated three-dimensional bioprinting and cryopreservation. *Int J Bioprint*. 2026:12(2):025500515. doi: 10.36922/IJB025500515

**Received:** December 10, 2025

**Revised:** January 20, 2026

**Accepted:** February 9, 2026

**Published online:** February 20, 2026



## Abstract

Three-dimensional (3D) bioprinting enables the fabrication of engineered tissues, but cell damage during printing and limitations in long-term preservation hinder practical applications. Traditional cryoprotectants, such as dimethyl sulfoxide (DMSO), introduce cytotoxicity and require complex removal, restricting immediate tissue usability. Here, we present an integrated extrusion-based bioprinting and DMSO-free antifreeze hydrogel strategy to produce cell-laden constructs with high post-thaw viability and proliferative capacity. Systematic optimization of bioink composition (6% L-proline with varying gelatin methacryloyl concentrations), extrusion parameters, and crosslinking conditions enabled high-fidelity scaffold fabrication while preserving cell viability and proliferation. Numerical simulations guided the maximum printable heights for fibers of different diameters, supporting construct scalability. Storing cell-laden 3D-printed scaffolds in cryovials at −80 °C effectively maintained high cell viability compared with alternative cooling protocols. Cells in 3D scaffolds exhibited superior post-thaw proliferation compared with two-dimensional culture, and the platform was validated using C2C12 myoblasts, achieving high survival and robust recovery of proliferative capacity. This study establishes a practical and versatile framework for integrating bioprinting and cryopreservation to support the generation of cell-laden constructs with preserved viability and structural integrity for regenerative medicine applications.

***Keywords:*** Three-dimensional bioprinting; Cryopreservation; Gelatin methacryloyl; Antifreeze hydrogel; Dimethyl sulfoxide-free hydrogels ; Printability optimization

## 1. Introduction

Three-dimensional (3D) bioprinting has become a transformative technology for fabricating functional tissues and organs by precisely depositing cell-laden bioinks into predefined architectures.[1,2] In recent years, this field has increasingly aligned with the concept of rational mechanical design of bio-metamaterials, in which structural architectures are deliberately engineered to regulate mechanical behavior and guide biological functions[3]. Within this context, the structural fidelity and biological functionality of printed constructs are highly dependent on the interplay between bioink properties, printing parameters, and quantitative structure–property–function relationships, as emphasized in advanced mechanostructure design frameworks.[4-7] Although extrusion-based bioprinting has advanced rapidly, the optimization of its key process parameters—such as extrusion pressure, printing speed, and nozzle diameter—remains incomplete.[8,9] These parameters collectively determine filament morphology, scaffold porosity, and mechanical integrity, directly influencing the reproducibility and biological performance of printed constructs.[10,11] Excessive shear stress generated during extrusion, particularly under high pressures or through fine nozzles, can compromise cellular membranes and viability.[12-14] Therefore, achieving a balance between printing precision and cytocompatibility is essential for constructing biofunctional tissues with high cell survival.

Beyond fabrication, the long-term preservation and "ready-to-use" capability of bioprinted tissues remain significant obstacles to their clinical translation. On-demand printing limits scalability, logistics, and availability for regenerative medicine applications.[15,16] The integration of cryopreservation with bioprinting offers a promising approach for off-site manufacturing and long-term storage.[17,18] However, freezing and thawing processes can cause osmotic imbalance and ice crystal formation, resulting in structural deformation and cell death. Consequently, cryoprotective optimization of bioinks is critical to maintain both scaffold fidelity and post-thaw cell function. Conventional cryoprotectants such as dimethyl sulfoxide (DMSO) and glycerol remain widely used, but their cytotoxicity and the need for complex removal procedures limit their applicability.[19-21] Previous studies have shown that although DMSO-based systems can preserve cell viability above 80%, residual toxicity and impaired cell functionality after thawing remain persistent concerns, underscoring the need for safer, low-toxicity alternatives.[22,23]

In this context, L-proline (L-Pro) has emerged as a superior natural alternative due to its low toxicity and multifaceted cryoprotective mechanisms. Thermodynamically, L-Pro interacts with water molecules via strong hydrogen bonds, lowering the crystallization temperature and promoting the formation of a glassy state (vitrification), thereby inhibiting ice crystal growth and minimizing mechanical damage.[24,25] Biologically, as a permeable osmoprotectant, it stabilizes the intracellular environment by binding to intracellular water; this mitigates the lethal increase in ionic strength during freezing and maintains electrolyte balance. Furthermore, acting as a molecular chaperone and antioxidant, it preserves cell membrane integrity, scavenges reactive oxygen species (ROS) to alleviate oxidative stress, and maintains protein structure and enzyme function.[26,27] These combined properties make L-Pro an ideal candidate for developing cytotoxicity-free cryoprotective bioinks.

To overcome the cytotoxic limitations of conventional cryoprotectants, our previous work established a low-toxicity L-Pro-based hydrogel platform that enabled DMSO-free, high-efficiency cryopreservation of 3T3 cells.[28] Building upon this foundation, the present study introduces an integrated bioprinting–cryopreservation strategy based on a gelatin methacryloyl (GelMA)/L-Pro composite hydrogel to address the longstanding challenge of long-term storage and preservation of cell-laden 3D bioconstructs. This platform systematically investigates the interplay between printing parameters, crosslinking strategies, and cryopreservation performance, with the goal of achieving structurally precise, highly viable cell-laden scaffolds with preserved proliferative capacity. Specifically, the printability and structural fidelity of GelMA/L-Pro bioinks were characterized under varying extrusion pressures, nozzle diameters, and printing speeds, leading to the identification of optimal, cell-compatible manufacturing parameters. Subsequent analyses evaluated post-printing cell viability and proliferation, as well as the effects of crosslinking method, cooling rate, and scaffold architecture on cryopreservation outcomes. Finally, C2C12 myoblasts were employed to validate the generalizability of the optimized hydrogel system across different cell types. Collectively, this work establishes a DMSO-free, printable antifreeze hydrogel framework that improves biocompatibility and preservation performance, thereby supporting the broader application of 3D bioprinting in tissue engineering and regenerative medicine.

## 2. Materials and methods

### 2.1. Materials

Gelatin methacryloyl (amino substitution: 60 %; molecular weight = 100–200 kDa; Polydispersity Index = 1.5–2), lithium phenyl (2,4,6-trimethylbenzoyl) phosphinate

(LAP), and GelMA lysis buffer were purchased from Suzhou Yongqinquan Intelligent Equipment Co., Ltd. (China). Dulbecco's modified Eagle medium, trypsin–ethylenediaminetetraacetic acid, and penicillin–streptomycin mixture were purchased from Gibco (United States). Acridine orange/propidium iodide (AO/PI) fluorescent dye was purchased from Guangzhou Broad Boju Technology Co., Ltd. (China). Cell Counting Kit-8 (CCK-8) reagent was purchased from Dojindo Chemical Co., Ltd. (Japan). L-Pro was purchased from Shanghai MacLean Biochemical Technology Co., Ltd. (China). Phosphate-buffered saline was purchased from Tianjin Haoyang Biotechnology Co., Ltd. (China), and South American fetal bovine serum (FBS) was purchased from Gemini Biotechnology Co., Ltd. (China). Extrusion-type biological 3D printer (BP6601) was purchased from Suzhou Yongqinquan Intelligent Equipment Co., Ltd. (China).

### 2.2. Characterization of antifreeze hydrogels

#### *2.2.1. Rheological analysis*

The rheological properties of the hydrogel solutions were evaluated using a rotational rheometer (Discovery HR-2, TA Instruments, United States) equipped with a 40 mm cone-and-plate geometry. To assess printability, flow sweep tests were performed at 25 °C. The viscosity was recorded as the shear rate increased logarithmically from 0.1 to 100/s. The sol–gel transition behavior and low-temperature storage modulus were characterized via oscillatory temperature sweeps. The temperature was ramped from 40 °C down to 4 °C and subsequently heated back to 40 °C at a rate of 5 °C/min. During the sweep, the strain and angular frequency were fixed at 1% and 5 rad/s, respectively. The sol–gel transition temperature was defined as the intersection point of the storage modulus (G′) and loss modulus (G″) curves.

#### *2.2.2. Swelling behavior*

The swelling kinetics were analyzed using a gravimetric method. Photocured hydrogel samples (dimensions: Φ 4 mm × 2 mm) were lyophilized and weighed to determine their initial dry weight ($W_d$). The dried samples were then immersed in PBS (pH 7.4) at 37 °C. At predetermined time intervals (0.25, 0.5, 1, 1.5, 2, 4, 6, 8, 10, and 12 h), the samples were retrieved, surface water was gently blotted with filter paper, and the samples were immediately weighed to record the swollen weight ($W_s$). The swelling ratio (SR) was calculated using **Equation (1)**:

$$SR = (W_s - W_d)/W_d \quad (1)$$

#### *2.2.3. Mechanical testing*

The mechanical strength of the photocured hydrogels was evaluated using a universal mechanical testing machine (Instron 5944, Instron, United States). Cylindrical samples (dimensions: Φ 4 mm × 2 mm) were placed between parallel compression platens and subjected to uniaxial compression at a constant strain rate of 3 mm/min until 50% strain was reached.

### 2.3. Effect of printing parameters on the fidelity of antifreeze hydrogel scaffolds

#### *2.3.1. Preparation of antifreeze hydrogels with different concentrations*

A total volume of 20 mL of PBS was added to a brown bottle containing the initiator LAP (0.05 g). The solution was heated in a water bath at 40–50 °C for 15 min, and was shaken several times during the process. Finally, the initiator standard solution (0.25% [*w*/*v*], 2.5 mg/mL) was obtained. Subsequently, 500 mg, 700 mg, and 1,000 mg of GelMA lyophilized material, respectively, were measured and placed in three 15 mL centrifuge tubes. Then, 600 mg of L-Pro was weighed and added to the three centrifuge tubes. Following this, 8 mL of the prepared initiator standard solution was added. The three centrifuge tubes were then placed in 37 °C hot water and shaken until the solid GelMA in the tubes was completely melted. An appropriate amount of initiator standard solution was added to adjust the final volume in the centrifuge tube to 10 mL. Subsequently, the following antifreeze hydrogels were prepared: 6% L-Pro + 5% GelMA, 6% L-Pro + 7% GelMA, and 6% L-Pro + 10% GelMA.

#### *2.3.2. Three-dimensional printing parameters of antifreeze hydrogels with different concentrations*

Taking 6% L-Pro + 5% GelMA hydrogel as an example, the printing process is described in detail. After filtering the prepared hydrogel using a 0.22 μm filter, the 6% L-Pro + 5% GelMA hydrogel was placed in a light-proof brown barrel that matches the printer. The barrel was then placed in a 4 °C refrigerator for five minutes to pre-cool the hydrogel into a "jelly state" that was easy to print. At the same time, the printing parameters (printing speed, printing layer height, extrusion pressure, nozzle diameter, and path spacing, etc.) were set in the printing software (EFL_PotatoE, version 1.2.1). The temperature of the low-temperature platform was set to the target temperature, and printing was performed after it stabilized. To facilitate subsequent data analysis, an experimental number was set

for each experimental group. The specific information is shown in Table 1.

**Table 1. Three-dimensional printing experiment groups**

| Group | Hydrogel composition | Nozzle size |
|---|---|---|
| G1 | 6% L-Pro + 5% GelMA | 25G (0.26 mm) |
| G2 | 6% L-Pro + 5% GelMA | 27G (0.21 mm) |
| G3 | 6% L-Pro + 7% GelMA | 25G (0.26 mm) |
| G4 | 6% L-Pro + 7% GelMA | 27G (0.21 mm) |
| G5 | 6% L-Pro + 10% GelMA | 25G (0.26 mm) |
| G6 | 6% L-Pro + 10% GelMA | 27G (0.21 mm) |

Abbreviations: GelMA: Gelatin methacryloyl; L-Pro: L-proline.

#### *2.3.3. Diameter of antifreeze hydrogel scaffolds with different concentrations*

Different scaffold structures were obtained by setting different printing parameters. The scaffolds were fabricated with a footprint of 12 mm × 12 mm, a 90° grid interlacing angle, and a 0.2 mm layer height. The printing process was systematically varied across three translation speeds (240, 300, and 360 mm/min) and a range of extrusion pressures (15 kPa, 20 kPa, 25 kPa, 30 kPa, 35 kPa, 40 kPa, 45 kPa, 50 kPa, and 55 kPa). The architectural integrity of the resulting constructs was qualitatively assessed and classified as either successful (√) or failure (×). A construct was strictly defined as successful only when it fulfilled the following three criteria: (i) continuous filament extrusion without breakage or fragmentation; (ii) clearly resolved interconnected pores with no evidence of premature filament fusion; (iii) stable vertical stacking characterized by high structural integrity without collapse. Constructs failing to meet any of these requirements were categorized as failed instances of printing. Subsequently, the filament diameters and pore size of the successful scaffolds were quantified using ImageJ software (ImageJ, version 1.52) to establish the quantitative relationship between processing parameters and resultant structural dimensions.

### 2.4. Numerical simulation of printable height of hydrogel scaffolds with different diameters

During printing, vertical heat transfer within the scaffold gradually diminishes with increasing construct height, leading to a progressive rise in temperature at the top layers. Once a critical height is reached, insufficient cooling results in loss of mechanical support and collapse of the scaffold. For the 6% L-Pro + 7% GelMA hydrogel, experimental observations indicated that when the material temperature exceeded 20 °C, gel-to-sol transition occurred, and structural integrity could no longer be maintained. Accordingly, scaffolds composed of 6% L-Pro + 7% GelMA were printed on a low-temperature platform set at 5 °C using a 25G nozzle, with varying extrusion pressures and a printing speed of 360 mm/min. The designed scaffold footprint was 12 mm × 12 mm. COMSOL Multiphysics (COMSOL Multiphysics, version 6.0) was employed to simulate heat transfer within scaffolds of different filament diameters to determine the maximum printable height for each condition. A solid heat transfer model was used to calculate temperature distributions within the hydrogel at different printing heights and time points. In the model, the temperature of the cold platform ($T_{plat}$) was set to 5 °C and the ambient air temperature ($T_{air}$) to 25 °C. The thermal conductivity of the hydrogel was set to 0.57 W/(m$^2$·K), and the specific heat capacity was set to 4.136 kJ/(kg·K). All additional thermal and physical parameters of the hydrogel, including density and related properties, were obtained from the literature[17] and are summarized in Table S1. Because heat is continuously dissipated from the scaffold surface to the surrounding air, vertical heat transport within the construct decreases with increasing height. Therefore, a temperature of 20 °C was defined as the critical threshold corresponding to the gel-to-sol transition of the hydrogel. By simulating constructs with increasing heights, the evolution of the 20 °C isotherm within the hydrogel was monitored. When the temperature at the top layer exceeded 20 °C under steady-state conditions, the height of the immediately lower layer was defined as the maximum printable height for that scaffold diameter. The detailed scaffold geometry and heat transfer boundary conditions are illustrated in Figure 1.

### 2.5. Optimization of printing parameters for cell-laden antifreeze hydrogel scaffolds

#### *2.5.1. Preparation of cell-loaded antifreeze hydrogels with different concentrations*

The prepared 6% L-Pro + 5% GelMA, 6% L-Pro + 7% GelMA, and 6% L-Pro + 10% GelMA antifreeze hydrogels were filtered using a 0.22 μm filter, and the antifreeze hydrogels of different concentrations were evenly mixed with 3T3 cells (Beyotime Biotechnology, China) at a density of 1 × 10$^5$ cells/mL and placed in a 37 °C water bath for use.

#### *2.5.2. Three-dimensional printing of cell-laden antifreeze hydrogels*

The mixture of antifreeze hydrogel and cells was placed in a brown, light-proof cartridge, which was then placed in a 4 °C refrigerator for five minutes before printing. The 6% L-Pro + 5% GelMA, 6% L-Pro + 7% GelMA, and 6% L-Pro + 10% GelMA antifreeze hydrogels were printed on a 5 °C cold stage using 25G and 27G needles at different extrusion pressures and a printing speed of 360 mm/min.

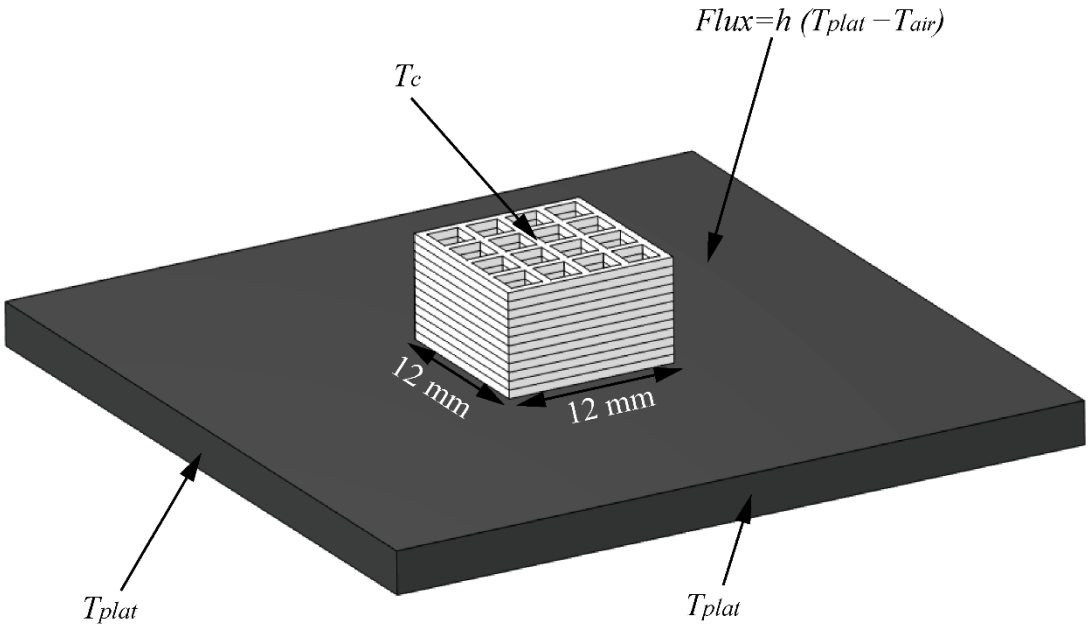


**Figure 1.** Bracket dimensions and boundary conditions for heat transfer simulation

Briefly, cell viability was assessed using the AO/PI dual fluorescent dye, and proliferation was evaluated using the CCK-8 assay, as detailed in the subsection. . Using the antifreeze hydrogels from the G3 group, 2-, 4-, 6-, 8-, 10-, and 12-layer hydrogel scaffolds containing 3T3 cells were printed at an extrusion pressure of 35 kPa and a printing speed of 360 mm/min to investigate the relationship between cell survival, proliferation capacity, and printing layer height. In addition, two-layer scaffolds were printed on cryogenic plates set at 15 °C, 10 °C, 5 °C, 0 °C, and −5 °C under the same printing conditions to assess the effect of cryogenic plate temperature on cell survival and proliferation.

The GelMA hydrogels were crosslinked by ultraviolet (UV) irradiation after adding a photoinitiator. As UV exposure may induce DNA damage, stress response, and oxidative stress, which may affect cell activity and function[29,30], two-layer G3 scaffolds printed at 5 °C were irradiated at a wavelength of 405 nm and an irradiance of 25 mW/cm$^2$ for 10, 30, 60, 120, and 180 s to evaluate the effect of UV exposure duration on cell survival and proliferation.

#### *2.5.3. Scaffold dissociation and cell recovery*

A standardized enzymatic digestion protocol, enhanced by mechanical agitation and thermal assistance, was employed to recover cells from the GelMA hydrogel constructs. The cell-laden hydrogels were finely minced and transferred into centrifuge tubes containing a 0.3 mg/mL GelMA lysis buffer. For the agitation-assisted group, the samples were incubated at 37 °C with gentle orbital shaking (60–80 rpm) for 15–30 min. Periodic manual pipetting was performed to accelerate matrix degradation. For the static control group, the fragmented hydrogels were incubated in the same digestion solution at 37 °C without agitation until complete dissociation was achieved. The resulting cell suspensions from all groups were centrifuged at 1,000 rpm for five minutes. The supernatant was discarded, and the cell pellets were resuspended in a complete culture medium for subsequent viability analysis.

#### *2.5.4. Quantitative viability and proliferation analysis*

Immediate post-thaw viability was quantified using a dual-fluorescence staining method. The cell suspension was mixed with AO/PI and analyzed using an automated JSY-SC-031N cell counter (Boda Boju Technology, Guangzhou, China). For longitudinal proliferation assessment, the recovered cells were normalized to a seeding density of 1 × 10$^5$ cells/mL and cultured in 96-well plates. The metabolic activity and proliferative kinetics were monitored by measuring the absorbance at 24, 48, and 72 h post-seeding using a microplate reader (SYNERGY H1 microplate reader, Thermo Fisher Scientific, USA). All assays were performed in triplicate to ensure statistical robustness.

### 2.6. Effect of cross-linking method on cryopreservation efficiency of cell-laden hydrogel scaffolds

3T3 cells at a density of 1 × 10$^5$ cells/mL were mixed evenly with 6% L-Pro + 7% GelMA antifreeze hydrogel.

After co-culture for three hours, two layers of scaffolds were printed on a 5 °C cryostat using a 25G needle, 35 kPa extrusion pressure, and a printing speed of 360 mm/min. After printing the cell-laden cryoprotectant hydrogel into the desired structure, the scaffold was placed in a 4 °C refrigerator for five minutes for low-temperature crosslinking. Alternatively, the printed scaffold was irradiated with a 405 nm wavelength curing light source with an irradiance of 25 mW/cm$^2$ for 60 s for UV crosslinking, followed by cryopreservation using F-2 cooling. After seven days of cryopreservation, the cryoprotectant hydrogel scaffolds in the crosslinked group were rewarmed in a 37 °C water bath to release the cells. In the UV crosslinked group, the crosslinked hydrogel scaffolds were lysed using GelMA lysis buffer to release the cells. Cells from each experimental group were collected and assayed for cell viability and proliferation.

### 2.7. Cryopreservation efficiency of cell-laden hydrogel scaffolds under different cooling protocols

3T3 cells at a density of $1 \times 10^5$ cells/mL were mixed evenly with 6% L-Pro + 7% GelMA cryoprotectant hydrogel and co-cultured for three hours. Two layers of scaffolds were then printed on a 5 °C cold stage using a 25G needle, 35 kPa extrusion pressure, and a printing speed of 360 mm/min. After the cell-laden cryoprotectant hydrogel was printed into the desired structure, it was placed in a 4 °C refrigerator for five minutes to achieve low-temperature crosslinking. The printed cell-laden scaffolds were placed in cryovials and stored in programmed cooling (F-1), a −80 °C freezer (F-2), and liquid nitrogen (F-3). In F-1', the 3D-printed cell-laden scaffolds were placed directly in a programmed cooling box, then cooled in a −80 °C freezer overnight. Subsequently, they were transferred to liquid nitrogen for long-term storage. In F-2', the 3D-printed cell-laden scaffolds were placed directly in a −80 °C freezer for three hours and then transferred to liquid nitrogen for long-term storage. In F-3', the 3D-printed cell-laden scaffolds were placed directly in liquid nitrogen for long-term storage. During rewarming, the scaffolds in F-1', F-2', and F-3' were quickly placed in centrifuge tubes and then heated in a 37 °C water bath with shaking. Temperature profiles were monitored using thermocouples interfaced with an Agilent (United States) 34970A data logger. The thermocouple probes were embedded within the hydrogel scaffolds, and data acquisition was performed throughout the cooling process according to freezing protocols F-1 through F-3'. Subsequently, the cryovials with the hydrogel scaffolds were placed in a 37 °C water bath for continuous agitation, during which temperature history was continuously recorded. The average cooling and warming rates were calculated over the temperature intervals of 0 °C to −60 °C and −196 °C to 37 °C, respectively. All cryopreservation protocol details are summarized in Table S2.

### 2.8. Cryopreservation efficiency of cell-laden hydrogel scaffolds of different volumes and structures, and the effects of different culture methods on cell proliferation

3T3 cells at a density of $1 \times 10^5$ cells/mL were mixed evenly with 6% L-Pro + 7% GelMA antifreeze hydrogels. After co-culture for three hours, two layers of scaffolds were printed on a 5 °C cold stage using a 25G needle, 35 kPa extrusion pressure, and a printing speed of 360 mm/min. After printing into the pre-defined structure, the cell-laden antifreeze hydrogels were cross-linked at low temperature with UV light. They were then cryopreserved using the F-2 cooling protocol. After seven days of cryopreservation, the antifreeze hydrogel groups were rewarmed in a water bath, centrifuged, and resuspended in complete culture medium before being plated in culture flasks for two-dimensional culture. For the UV-crosslinked group, the cell-laden hydrogel scaffolds were rewarmed in a water bath and plated in 6-well plates. Complete culture medium was then added to the wells for 3D culture. Cell viability and proliferation were assessed by lysing the scaffolds with a lysis buffer to release the cells.

### 2.9. Cryopreservation efficiency of C2C12 myoblasts by antifreeze hydrogels

C2C12 myoblasts (Beyotime Biotechnology, China) were suspended in four distinct hydrogel prepolymer solutions (7% GelMA, 6% L-Pro + 5% GelMA, 6% L-Pro + 7% GelMA, and 6% L-Pro + 10% GelMA) at a final density of $1 \times 10^5$ cells/mL and incubated at 37 °C for three hours. Subsequently, the cell-laden bioinks were fabricated into bilayer scaffolds (12 mm × 12 mm) via extrusion bioprinting (nozzle: 25G; pressure: 35 kPa; speed: 360 mm/min). Following fabrication, the scaffolds were equilibrated at 4 °C for five minutes and then cryopreserved according to the F-2 protocol. As a positive control, C2C12 cells ($1 \times 10^5$ cells/mL) suspended in 10% DMSO were subjected to the same freezing cycle. Post-thaw cell viability was assessed immediately, while proliferation kinetics were quantified after 24, 48, and 72 h of culture.

### 2.10. Statistical analysis

All experimental data are expressed as mean ± standard deviation, and all the experiments were performed in triplicate. Data were analyzed using one-way analysis of variance and Tukey's multiple comparisons test in GraphPad Prism 9. The statistical significance was set as: ns, no significant; $^*p < 0.05$; $^{**}p < 0.01$; $^{***}p < 0.001$; and

$^{****}p < 0.0001$.

## 3. Results and discussion

### 3.1. Three-dimensional printing of gelatin methacryloyl scaffolds with tunable shapes and structural complexity

Figure 2 presents a series of hydrogel scaffolds fabricated using GelMA as the bioink. Figure 2A–C illustrates three representative single-layer constructs—cylindrical, cubic, and cobweb-like scaffolds. These structures were formed through low-temperature physical gelation, which enabled rapid stabilization of the extruded filaments and maintained the designed pore geometry. The clear differences in architecture demonstrate the ability of GelMA to support both regular (cubic, cylindrical) and complex (cobweb-like) patterning. Figure 2D,E displays multi-layered cubic scaffolds, which were subsequently crosslinked using UV irradiation to achieve enhanced mechanical stability and maintain vertical stacking integrity. Figure 2E confirms that the printed filaments retain uniform diameter and layer alignment during vertical buildup, indicating the good printability and shape-retention properties of GelMA under optimized printing parameters. Collectively, these results demonstrate that GelMA is a highly adaptable bioink capable of forming both simple and complex architectures through physical gelation and photo-crosslinking. In combination with the BP6601 extrusion-type bio-3D printer, this system enables the fabrication of customized, high-resolution scaffolds suitable for diverse tissue-engineering applications.

### 3.2. Rheological and mechanical properties suitability validation for extrusion-based bioprinting

Figure 3 illustrates the rheological and physical properties of the antifreeze hydrogel formulations. In the viscosity analysis (Figure 3A), the initial viscosity exhibited a positive correlation with increasing GelMA concentration. The 6% L-Pro + 10% GelMA group displayed the highest viscosity (0.018 Pa·s), followed by the 6% L-Pro + 7% GelMA (0.011 Pa·s) and 6% L-Pro + 5% GelMA (0.007 Pa·s) groups. Crucially, as shown in Figure 3B, all groups demonstrated characteristic shear-thinning behavior, where viscosity decreased significantly with increasing shear rate. This property indicates their suitability for extrusion-based bioprinting by minimizing flow resistance. A corresponding trend was observed in the mechanical evaluation (Figure 3C), where the elastic modulus increased significantly with GelMA concentration. This structural reinforcement was further reflected in the swelling kinetics (Figure 3D); although all groups showed rapid water uptake within the first two hours, the 6% L-Pro + 10% GelMA group exhibited the lowest equilibrium swelling ratio. This inverse relationship is likely attributed

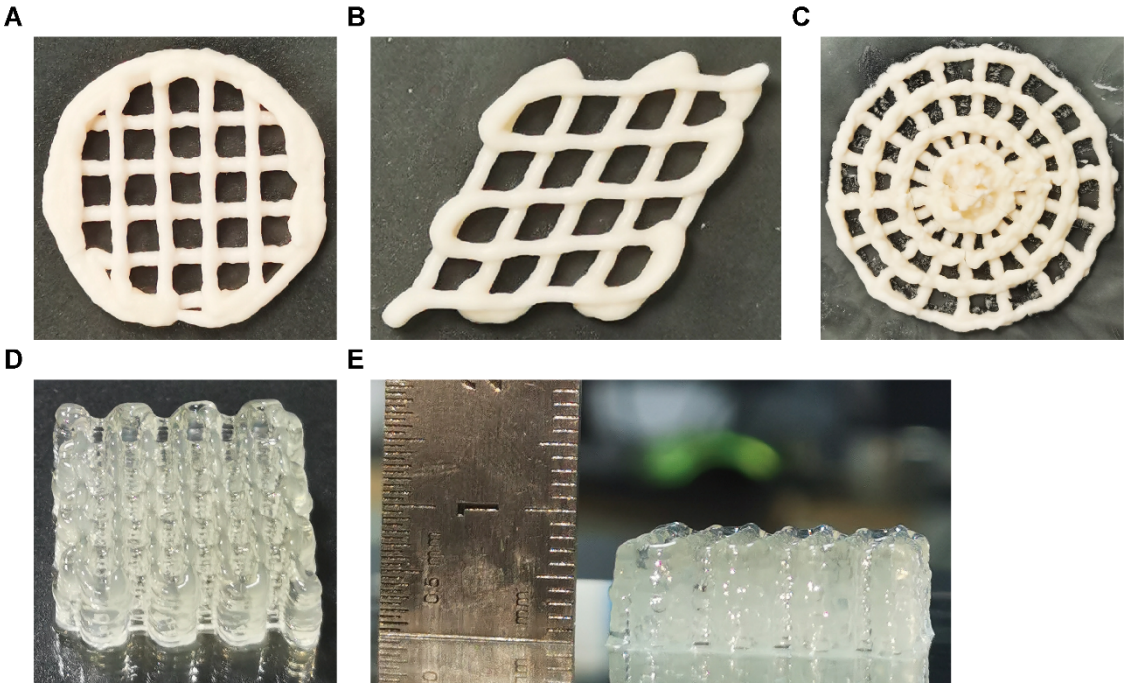


**Figure 2.** Hydrogel scaffolds of various geometries printed using gelatin methacryloyl as the bioink. (A) Cylindrical, (B) cubic, and (C) cobweb-like scaffold. (D) Multi-layer cubic scaffold. (E) Side view of the multi-layer cubic scaffold.

to the formation of a denser photocrosslinked network at higher polymer concentrations, consistent with established principles of hydrogel mechanics, where tighter mesh sizes restrict solvent penetration. Furthermore, the sol–gel transition temperatures (Figure 3E) for the 10%, 7%, and 5% GelMA groups were approximately 22 °C, 20 °C, and 17 °C, respectively, confirming that higher GelMA concentrations result in elevated transition temperatures. In summary, these results provide physical validation for the L-Pro/GelMA bioink, demonstrating that material stiffness, swelling behavior, and printability can be precisely tailored to balance structural fidelity with the specific mechanical requirements of the target tissue.[31,32]

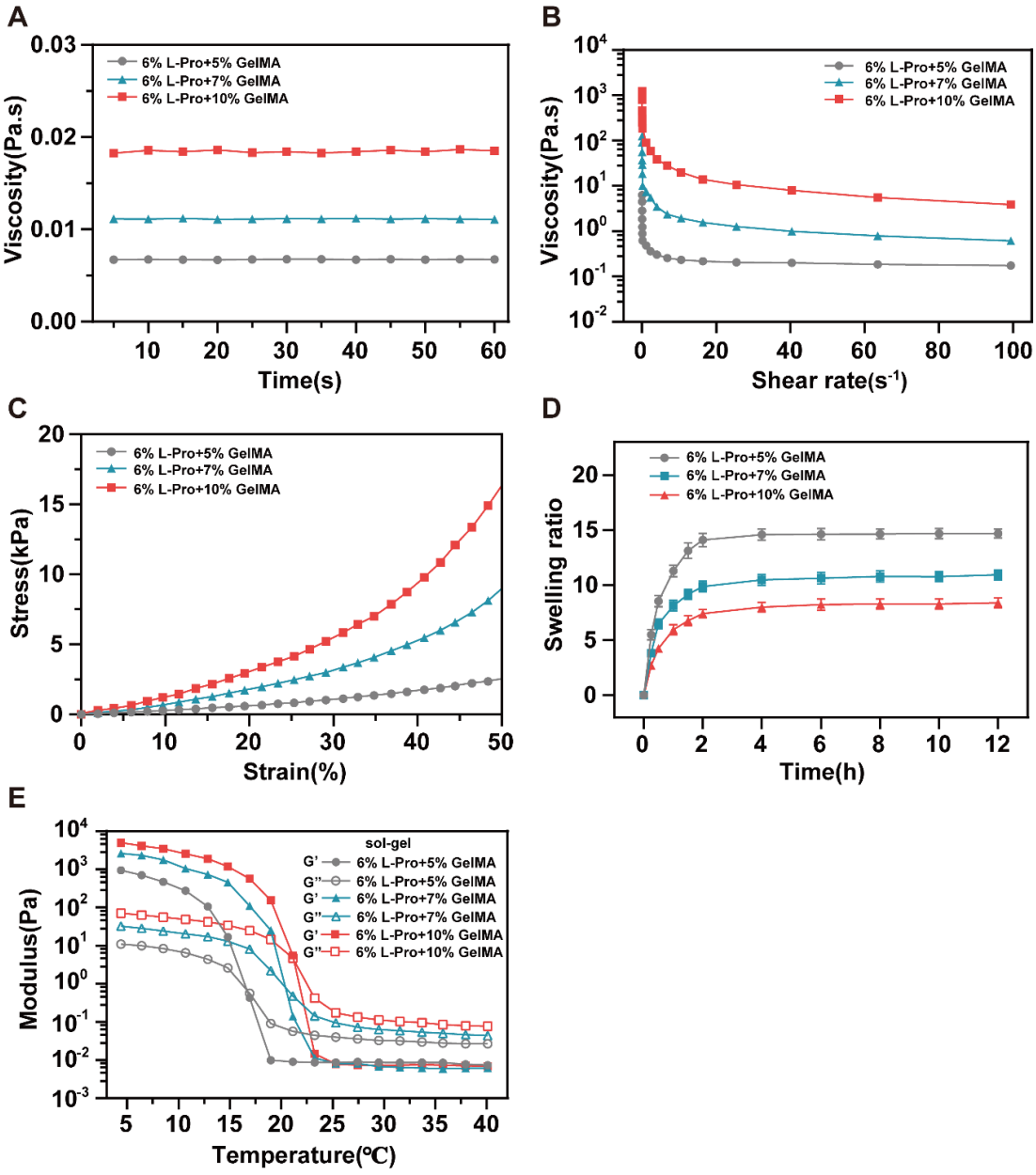


**Figure 3.** Physical and rheological characterization of the antifreeze hydrogels. (A) Viscosity measurements and (B) shear-thinning behavior of the different hydrogel groups. (C) Compressive modulus indicating the mechanical stiffness. (D) Swelling ratio of the hydrogels in phosphate-buffered saline over time. Data are presented as mean ± standard deviation ($n$ = 3 independent experiments for each condition). (E) Sol–gel transition assessed by rheological temperature sweeps.
Abbreviations: GelMA: Gelatin methacryloyl; L-Pro: L-proline.

### 3.3. Effects of extrusion pressure, nozzle size, and printing speed on the fidelity and diameter of the hydrogel scaffolds

The printability of the hydrogel bioinks was governed by a dynamic interplay between extrusion pressure, nozzle orifice size, and translation speed (Figure 4). For the G1 group, structurally integrated scaffolds were achieved within a pressure window of 25–40 kPa at speeds of 240–300 mm/min, and 30–45 kPa for 360 mm/min. Sub-optimal pressures resulted in discontinuous filaments due to insufficient material flow, whereas excessive pressures (>45 kPa) induced over-extrusion and compromised structural fidelity. The G2 group, utilizing a finer 27G nozzle, yielded reduced filament diameters under equivalent pressures, a phenomenon attributed to the increased hydraulic resistance within the smaller nozzle lumen (Figure S1).

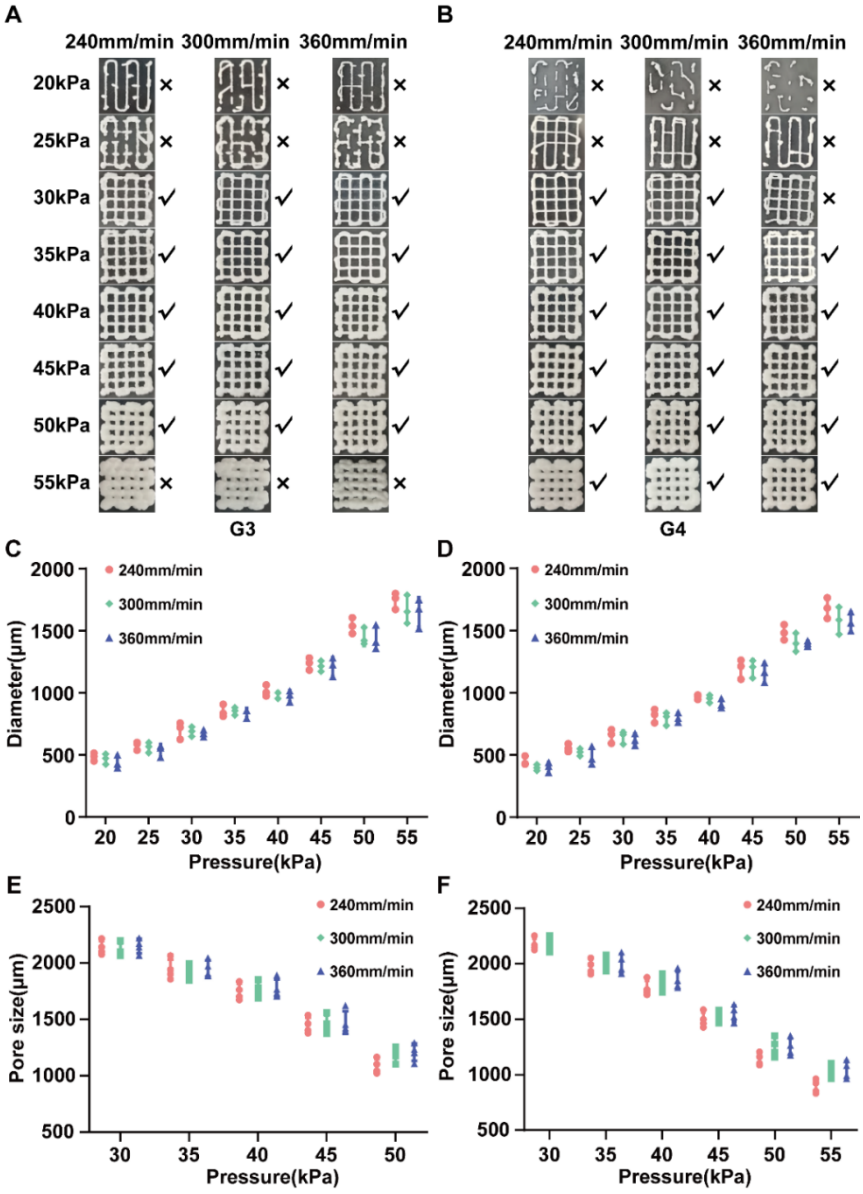


**Figure 4.** Effects of extrusion pressure, nozzle size, and printing speed on scaffold fidelity and structural dimensions of GelMA-based hydrogels with different concentrations. (A, B) Representative images of printed scaffolds fabricated from the G3 and G4 groups under varying printing conditions. (C, D) Quantitative analysis of scaffold filament diameter for G3 and G4, respectively. (E, F) Quantitative analysis of pore size for G3 and G4, respectively. Data are presented as mean ± standard deviation (diameter: $n = 3$ independent prints per condition; pore size: $n = 4$ independent prints per condition).
Note: √ indicates success and × indicates failure.
Abbreviations: GelMA: Gelatin methacryloyl; L-Pro: L-proline.

For the G3 (7% GelMA) and G4 (higher GelMA content) groups, the stable printing windows shifted to 30–50 kPa and 35–55 kPa, respectively. The higher viscosity and shear modulus of G4 necessitated elevated pressures to maintain continuous extrusion; however, this increased concentration significantly enhanced structural fidelity compared to the more dilute formulations. In groups G5 and G6, the minimum pressure threshold for structural completeness positively correlated with printing speed (Figure S2). At elevated pressures, the risk of over-extrusion was partially mitigated by higher speeds, which reduced the material deposition volume per unit area. These observations underscore the delicate balance between rheological properties and process parameters required to achieve reproducible scaffold geometries[33,34,35].

Quantitative analysis of filament diameters further revealed that extrusion pressure exerted a more pronounced effect on morphology than printing speed (Figure 4C,D). For instance, in group G1 at 30 kPa, increasing the speed from 240 to 360 mm/min reduced the filament diameter by approximately 21%, while increasing pressure from 15 to 45 kPa at 360 mm/min produced a fourfold increase in diameter (Figure S1). This trend was consistent across groups G2–G6, where increasing GelMA concentration (from 5% to 10%) led to higher bioink viscosity, thereby requiring higher extrusion forces and yielding broader filaments. These results demonstrate that higher bioink viscosities correlate with increased shear resistance and enhanced filament stability.[36]

Concurrent with the filament analysis, the scaffold pore size exhibited a significant negative correlation with extrusion pressure across all groups. In group G3, the mean pore size decreased from approximately 2,150 μm at 30 kPa to 1,100 μm at 50 kPa (Figure 4E). This reduction is directly attributable to the expansion of filament width under elevated pressure, which encroaches upon the predefined grid spacing. Group G4 displayed a similar trend, with pore sizes decreasing from 2,180 μm to ~960 μm as pressure increased to 55 kPa (Figure 4F). Similar variation patterns were observed in groups G1/G2 and G5/G6 (Figures S1 and S2), confirming the universality of this relationship regardless of hydrogel concentration.

Ultimately, while hydrogel concentration determines the baseline rheological resistance, extrusion pressure and printing speed serve as the primary modulators of scaffold porosity. Precise control over the internal porous network is essential for facilitating efficient nutrient diffusion and metabolic waste clearance, which are critical for the biological performance of cell-laden constructs during long-term culture and post-thaw recovery.

### 3.4. Numerical simulation of printable height of hydrogel scaffolds with different diameters

Numerical simulations of transient cooling revealed the thermal limitations governing scaffold fabrication (Figure 5). Specifically, for a 600 μm scaffold, the 20 °C isotherm propagated to 6.0–6.6 mm within 240 s and plateaued at 7.2 mm by 600 s, establishing 7.2 mm as the theoretical maximum height. For a 900 μm scaffold, the isotherm reached 9.0 mm at 600 s, with layers below 6.3 mm cooling rapidly (< 300 s). To experimentally validate these COMSOL predictions, multi-layered scaffolds (filament diameter: 900 μm; base: 12 mm × 12 mm) were fabricated via extrusion 3D printing on a 5 °C cooling stage. The experimental outcomes closely mirrored the simulation: scaffolds printed to a height of 9.0 mm maintained structural stability, whereas increasing the height to 9.9 mm resulted in structural instability and collapse (Figure S3). This failure at 9.9 mm empirically confirms the simulated thermal threshold. For larger diameters (1200 μm), while the maximum theoretical height increased to 10.8 mm, the upper layers required prolonged cooling (up to 1,800 s). Collectively, these results highlight a critical trade-off: while larger diameters permit greater build heights, they increase thermal inertia, delaying cooling in upper layers. Such prolonged cooling kinetics can compromise crosslinking efficiency and structural uniformity. Although our model assumes post-print cooling rather than simultaneous deposition and curing, the Fourier's law of heat conduction provides a robust estimation of the thermal limits in cryogenic bioprinting, offering essential guidelines for balancing extrusion mechanics with heat transfer kinetics.

### 3.5. Effects of different printing conditions on cell survival rate

The influence of extrusion conditions on post-printing cell survival is presented in Figure 6. For the G1 group, cell viability remained above 95% across the pressure range of 15–45 kPa, showing no significant difference compared to non-printed controls (Figure S5). The G2 group, processed with a finer nozzle, exhibited a modest decrease in viability to 93.97% at 45 kPa, reflecting the impact of increased shear stress, yet survival remained within a high range (Figure S5). Similarly, G3 and G4 maintained high viability up to 45 kPa but showed significant reductions when pressure exceeded 50 kPa. In contrast, the more concentrated formulations (G5 and G6) displayed sharper declines: G5 dropped from 98.63% (control) to 81.49% at 55 kPa, while G6 maintained control-level viability only at ≤35 kPa, falling to 80.39% at 55 kPa (Figure S6).To provide a quantitative mechanistic understanding of these trends, particularly for the optimized G3 group, we estimated the

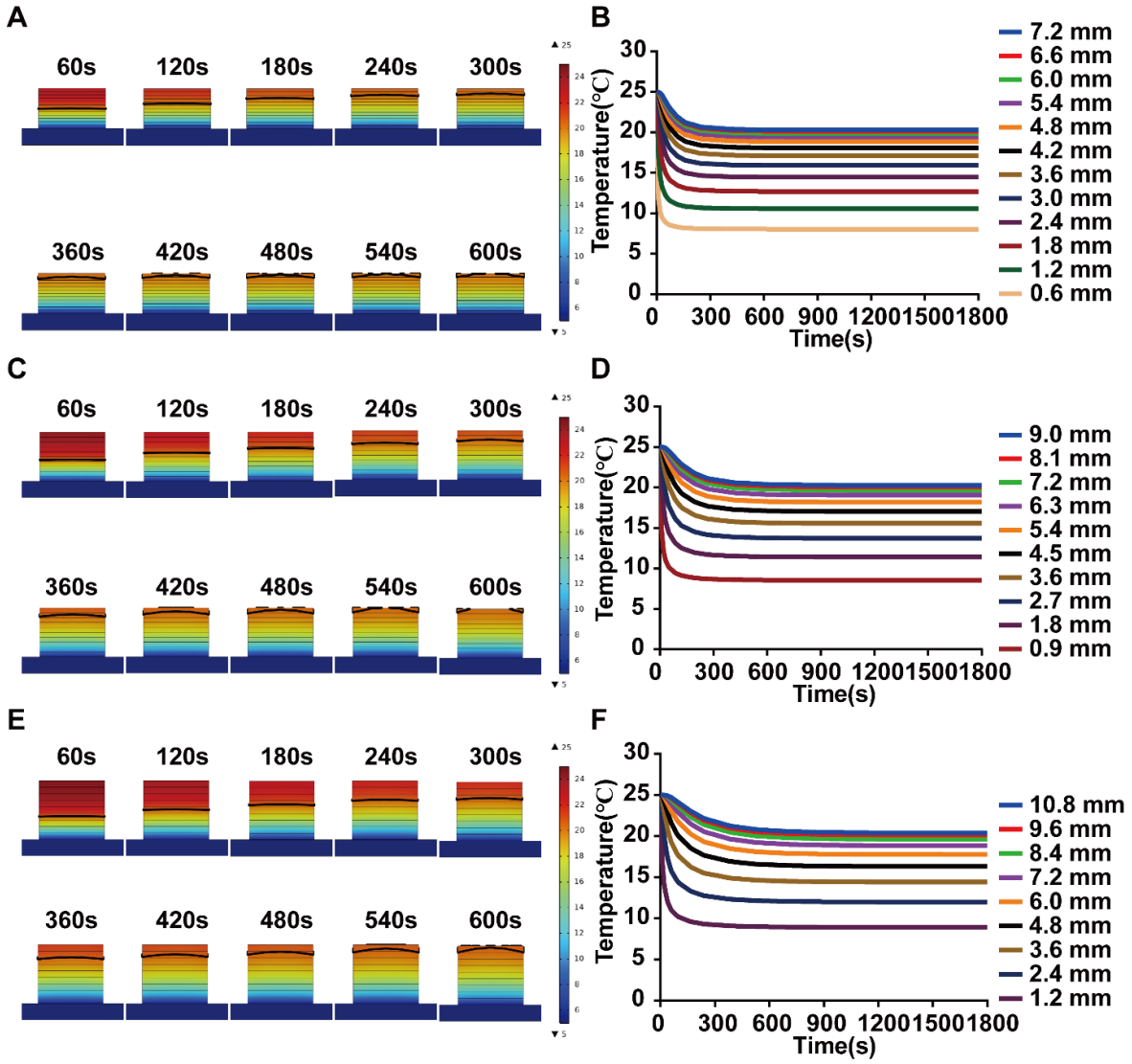


**Figure 5.** Heat transfer simulations of multilayer G3 scaffolds with different diameters. (A, C, E) Temperature contour maps of scaffolds with diameters of 600, 900, and 1,200 μm, respectively. (B, D, F) Corresponding temporal temperature profiles during printing.

maximum wall shear stress ($\tau_w$) acting on the cells using a simplified capillary flow model in **Equation (2)**:

$$\tau_w = R^*\Delta P/2/L \quad (2)$$

where R is the nozzle radius, ΔP is the pressure drop, and L is the nozzle length[37]. As summarized in Table 2, the calculated $\tau_w$ increased linearly with extrusion pressure. For the G3 formulation, the theoretical maximum $\tau_w$ was estimated to be approximately 119 Pa. This value is orders of magnitude lower than the critical threshold typically associated with massive shear-induced cell damage (≈5 kPa)[38], confirming that our optimized printing parameters generate a mild mechanical environment. This quantitative analysis effectively rationalizes the high post-printing cell viability (>90%) observed in the G3 group. Collectively, these results establish a clear correlation between hydrogel composition, extrusion mechanics, and cell survival. While extrusion pressure is a direct determinant of shear stress, GelMA concentration emerged as the critical intrinsic factor. Higher concentrations significantly increased the hydrogel modulus (e.g., 6,073 Pa at 10% vs. 1,296 Pa at 5% GelMA), thereby necessitating higher extrusion forces that subject encapsulated cells to greater shear.[39] As corroborated by our calculated stress values and viability data, while structural fidelity benefits from higher viscosity, bioink formulations must be optimized to balance mechanical strength with cellular protection to ensure bioprinting success.

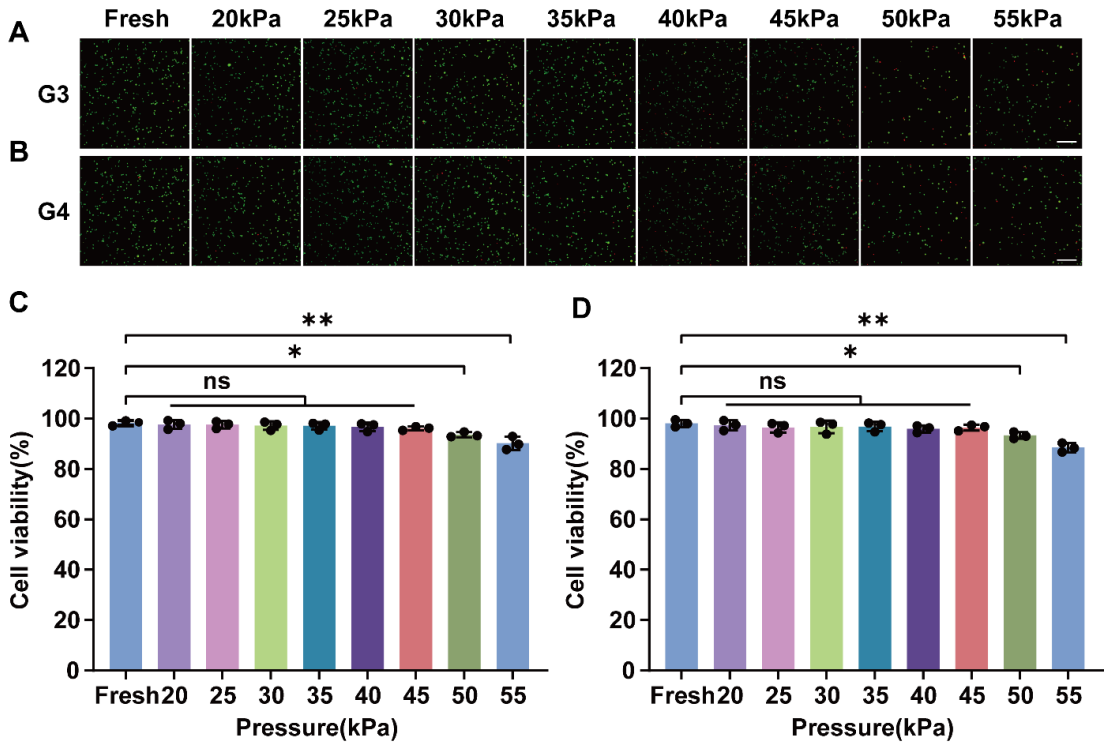


**Figure 6.** Cell viability of 3T3 fibroblasts under different printing conditions. (A, B) Representative live/dead fluorescence images (acquired using an automated cell counter with imaging capability as part of routine cell counting and viability assessment) of constructs printed with the G3 and G4 groups, respectively. Scale bar: 100 μm; magnification: 20×. (C, D) Quantitative analysis of cell viability for G3 and G4 under varying printing conditions. Data are presented as mean ± standard deviation ($n$ = 3 independent experiments for each condition; *$p$ < 0.05, **$p$ < 0.01, ns: not significant).

**Table 2. Estimated maximum wall shear stress for the G3 bioink**

| R (m) | ΔP (Pa) | L (m) | $\tau_w$ (Pa) |
|---|---|---|---|
| 0.00013 | 20,000 | 0.03 | 43.33333333 |
| 0.00013 | 25,000 | 0.03 | 54.16666667 |
| 0.00013 | 30,000 | 0.03 | 65 |
| 0.00013 | 35,000 | 0.03 | 75.83333333 |
| 0.00013 | 40,000 | 0.03 | 86.66666667 |
| 0.00013 | 45,000 | 0.03 | 97.5 |
| 0.00013 | 50,000 | 0.03 | 108.3333333 |
| 0.00013 | 55,000 | 0.03 | 119.1666667 |

### 3.6. Effects of different printing conditions on cell proliferation

The proliferation of encapsulated cells in G3 and G4 hydrogels over 48 h is shown in Figure 7. In the G3 group, optical density values at 24 h for cells printed at 30, 35, and 50 kPa were slightly lower than those of the fresh control, but no statistically significant differences were observed across extrusion pressures. By 48 h, all pressure groups exhibited comparable proliferative activity to the fresh control, indicating rapid recovery from transient extrusion-induced stress. A similar trend was observed in the G4 group, where optical density values at higher pressures (40–55 kPa) were moderately reduced at 24 h, though all values remained above 0.9. After 48 h, OD values in all groups exceeded 0.95, confirming re-established growth kinetics. These results extend the viability findings in Figure 6 by showing that cells not only survived but also retained proliferative potential post-extrusion. The transient suppression of proliferation at 24 h likely reflects acute shear-induced stress during extrusion, consistent with prior reports of temporary cell cycle arrest or delayed metabolism.[40] The subsequent recovery by 48 h underscores the resilience of encapsulated cells within GelMA microenvironments. Moreover, the observation that both 5% and 7% formulations preserved proliferative activity suggests that moderate polymer concentration increases do not hinder long-term cell growth, provided extrusion parameters are appropriately controlled. Collectively, these results support the preservation of post-printing cellular viability and proliferative potential within GelMA-based antifreeze hydrogels, highlighting their suitability for applications requiring stable cell growth during subsequent *in vitro* culture.

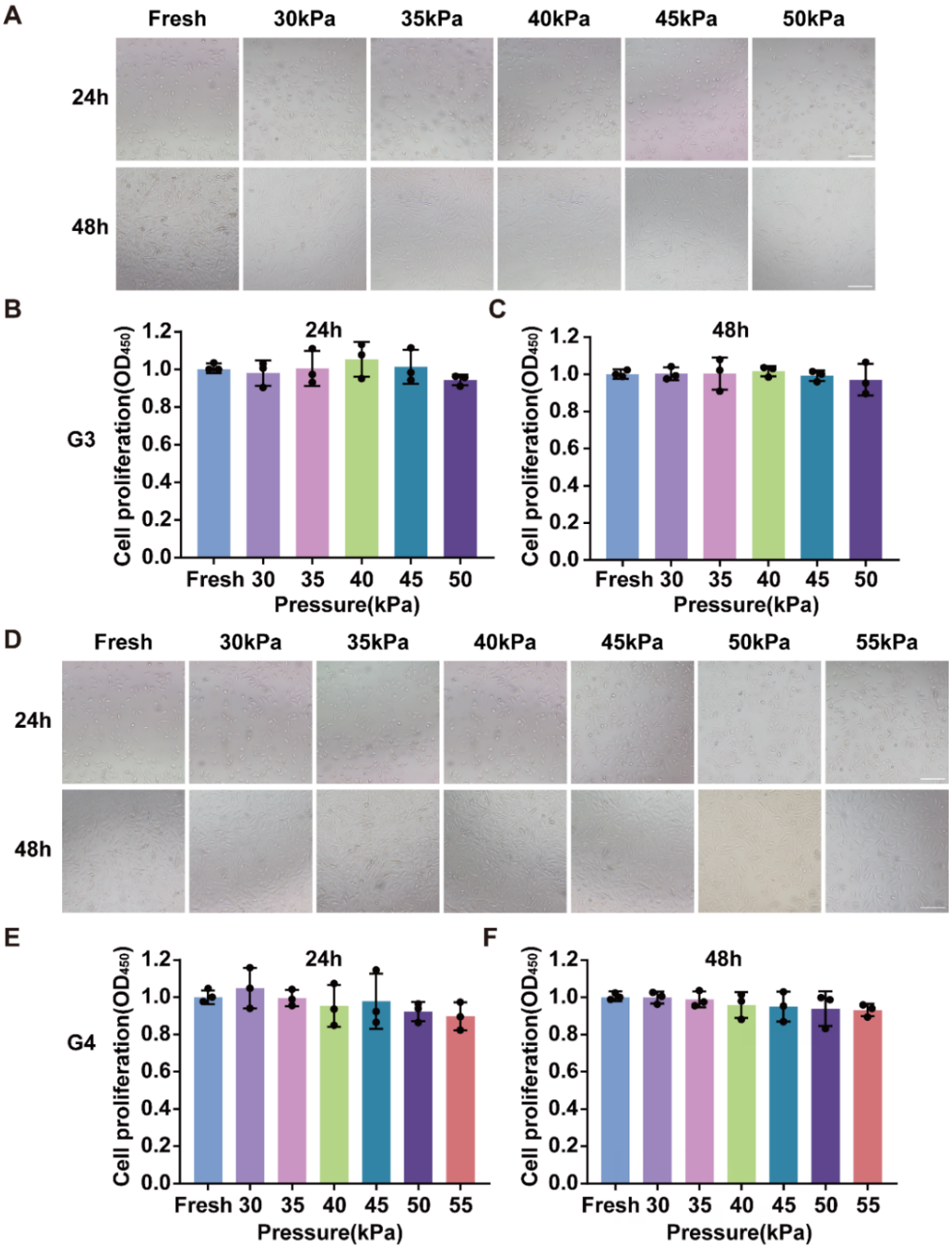


**Figure 7.** Proliferation rate of 3T3 cells in G3 and G4 groups after three-dimensional printing. (A) Cell proliferation images of G3 group, (B) 24-h cell proliferation of G3 group, (C) 48-h cell proliferation of G3 group, (D) cell proliferation images of G4 group, (E) 24-h cell proliferation of G4 group, (F) 48-h cell proliferation of G4 group. Scale bar: 100 μm; magnification: 20×. Data are presented as mean ± standard deviation ($n$ = 3 independent experiments for each condition).

### 3.7. Effects of scaffold height, cooling plate temperature, and ultraviolet crosslinking duration on cell viability and proliferation

To evaluate construct-scale influences, we examined multilayer scaffolds under varying environmental conditions (Figure 8). Increasing scaffold height (2–12 layers) did not significantly reduce cell viability or proliferation, demonstrating that multilayer stacking per se does not impair cellular function when printing parameters are optimized. This agrees with diffusion-based models showing that nutrient and oxygen transport remain adequate in relatively thin constructs.[41] By contrast, the cooling stage temperature exerted a more pronounced effect. Printing at 15–5 °C preserved high viability (>96%), whereas lower temperatures (0 °C, −5 °C) reduced survival to 91–94%, accompanied by transient metabolic suppression. These effects reflect cold-induced stress responses, including changes in membrane fluidity and ion fluxes, but were reversible within 48 h, suggesting that sub-zero printing remains feasible if carefully controlled. Finally, UV crosslinking introduced delayed but significant cytotoxicity. While immediate viability remained high across all exposure times, proliferation was suppressed at ≥120 s, consistent with ROS generation and DNA damage.[42] These results emphasize that excessive UV exposure compromises long-term function, even when short-term survival appears unaffected. Thus, crosslinking protocols should minimize irradiation time to balance structural fidelity with cell safety. Collectively, the results of Figure 8 demonstrate that structural complexity (scaffold height) does not compromise cell survival or growth, whereas environmental factors, such as plate temperature and UV crosslinking time, exert more pronounced effects.

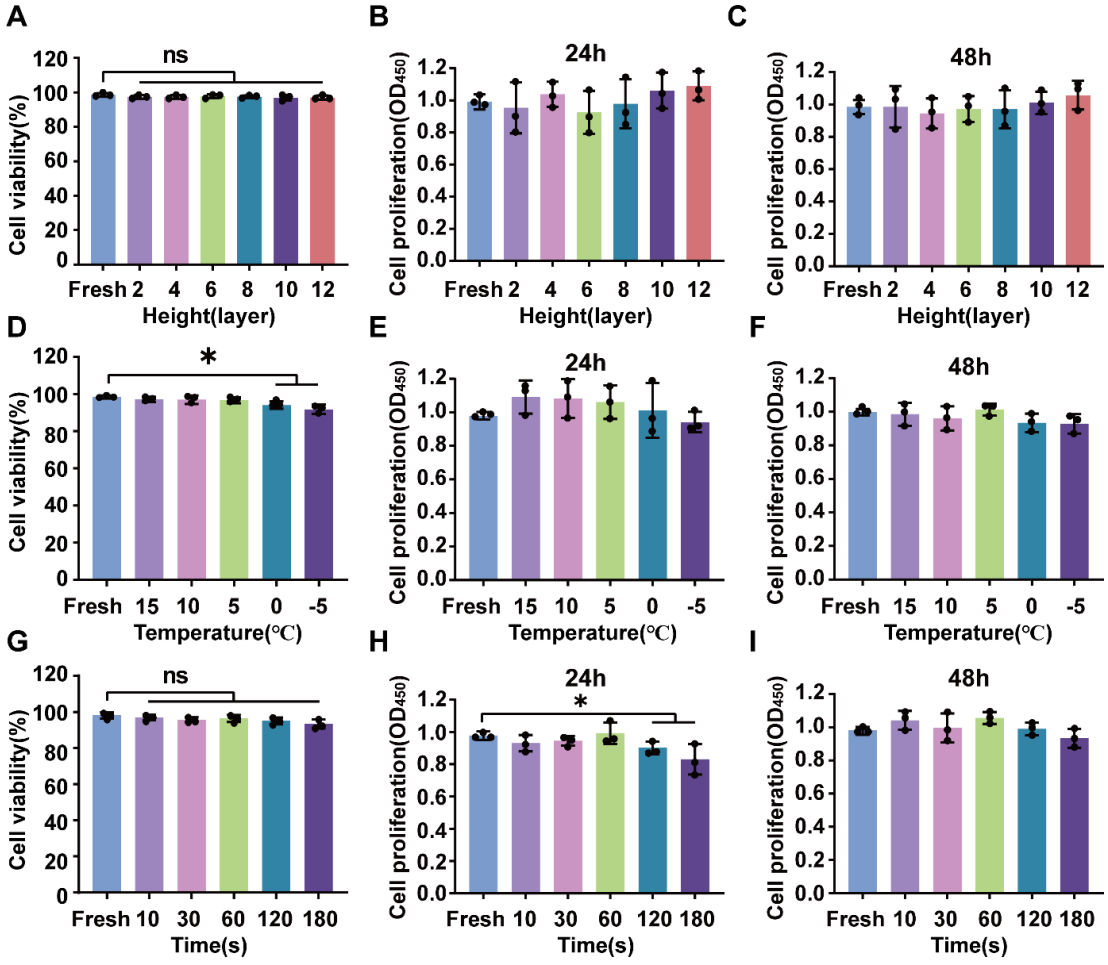


**Figure 8.** Cell survival and proliferation rates under different printing conditions. (A) Cell survival rate with different scaffold layer numbers. (B) Cell proliferation rate at 24 h. (C) Cell proliferation rate at 48 h. (D) Cell survival rate at different cryogenic cooling stage temperatures. (E) Cell proliferation rate at 24 h. (F) Cell proliferation rate at 48 h. (G) Cell survival rate at different ultraviolet irradiation times. (H) Cell proliferation rate at 24 h. (I) Cell proliferation rate at 48 h. Data are presented as mean ± standard deviation ($n = 3$ independent experiments for each condition; $^*p < 0.05$, ns: not significant).

### 3.8. Effect of cross-linking method on cryopreservation efficiency of cell-laden hydrogel scaffolds

To ensure that the recovery process itself did not introduce experimental bias, we performed a baseline analysis on the unfrozen control group. As shown in Figure 9A,B, both the frozen crosslinking group (91.71%) and the UV crosslinking group (90.45%) exhibited high and nearly identical cell viability after scaffold dissociation, with statistical analysis confirming no significant difference between the groups. These results validate that our optimized agitation-assisted digestion protocol provides stable and efficient cell recovery. As illustrated in Figure S8, which presents the optimization of the enzymatic digestion protocol for enhanced cell recovery, the agitation-assisted dissociation group showed a significantly higher cell viability compared with the static method. Representative live/dead staining images (Figure S8A) highlight the predominance of live cells in the agitation-assisted group, while quantitative analysis (Figure S8B) confirms the improved recovery efficiency.Following this baseline validation, we assessed the post-thaw performance of the bioprinted constructs. As illustrated in Figure 9C, both groups maintained high post-thaw cell survival, with a predominance of viable cells (green fluorescence). Quantitative analysis (Figure 9D) confirmed comparable viability between the cryo-cycled (70.89%) and UV-crosslinked (73.13%) groups, with no statistically significant difference. These findings suggest that the crosslinking strategy does not fundamentally dictate cryopreservation efficiency, consistent with prior studies highlighting the dominant roles of cryoprotectant formulation and cooling–warming kinetics. However, the two strategies offer distinct advantages for downstream applications. The cryo-crosslinked hydrogels exhibit a reversible gel–sol transition, facilitating rapid and non-invasive cell recovery for cell banking. In contrast, retrieving cells from UV-crosslinked networks requires enzymatic degradation; while not inherently cytotoxic, this process is time-consuming. Consequently, the reversible cryo-cycling approach represents a more practical and biocompatible strategy for cell retrieval, whereas the UV-crosslinked hydrogels provide a stable microenvironment, making them the superior choice for post-thaw 3D tissue culture.

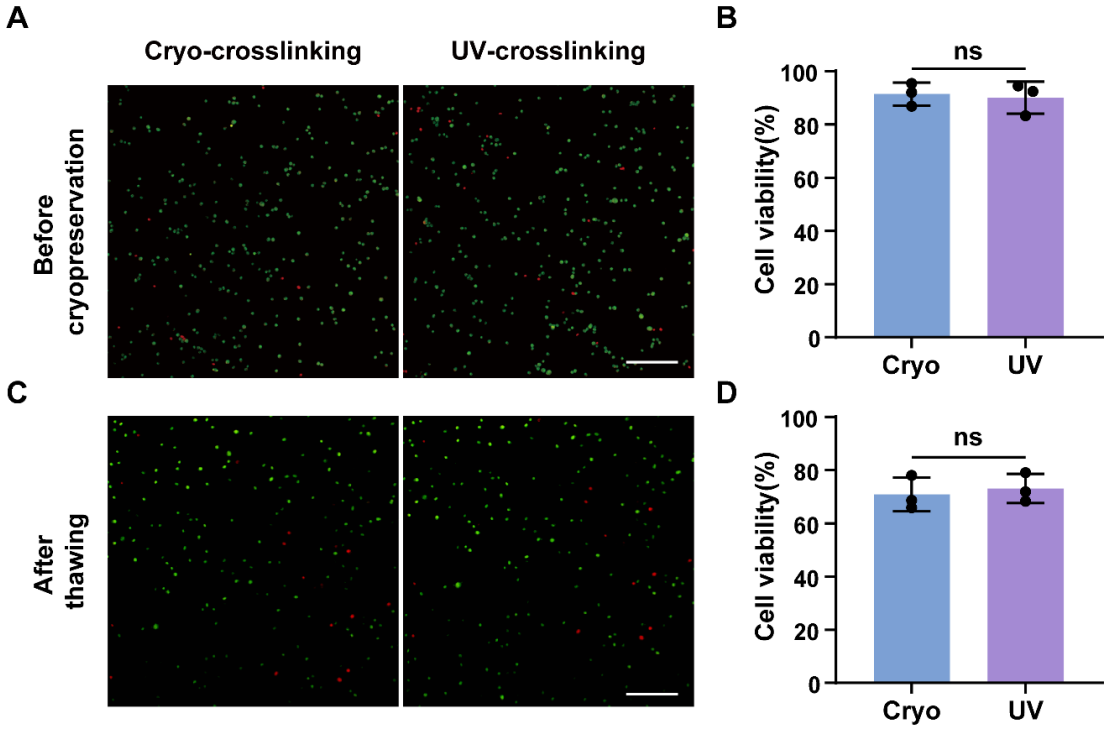


**Figure 9.** Validation of cell recovery consistency and post-thaw viability across different crosslinking modalities. (A) Live/dead fluorescence images of cells before cryopreservation. (B) Cell viability after dissociation. Scale bar: 100 μm; magnification: 20×. (C) Live/dead fluorescence images of cells after thawing. Scale bar: 100 μm; magnification: 20×. (D) Cell viability after thawing. Data are presented as mean ± standard deviation ($n$ = 3 independent experiments for each condition; ns: not significant).
Abbreviations: UV: Ultraviolet.

### 3.9. Cryopreservation efficiency of cell-laden hydrogel scaffolds with different cooling methods

Figure 10A shows that post-thaw viability varied significantly across six cooling protocols, with F-2 yielding the highest survival (70.52%) and F-3' the lowest (16.24%). Quantitative analysis (Figure 10B) confirmed this trend, with intermediate viabilities for F-1 (43.88%), F-3 (39.87%), F-1' (49.18%), and F-2' (54.56%). Statistical analysis indicated no difference between F-1 and F-1', whereas direct freezing without cryotube placement improved the survival rates of F-2' and F-3' compared to their respective cryotube-based controls. These results highlight the critical role of cooling rate in determining cryopreservation success. The superior outcome of F-2 likely arises from enhanced vitrification and reduced ice crystallization. These observations align with the "two-factor hypothesis" of cryoinjury, which posits that rapid cooling minimizes solute effects, while slow cooling promotes ice formation.[43] Thus, optimizing cooling dynamics—particularly the rates of cooling and warming—together with hydrogel-mediated cryoprotective agent delivery, is essential for maximizing post-thaw viability in scaffold-based cryopreservation.

### 3.10. Cryopreservation efficiency of cell-laden hydrogel scaffolds with different volumes and structures, and the effects of different culture methods on cell proliferation

Figure 11A shows that post-thaw viability of cells in printed fibers and multilayer scaffolds remained comparable across bioink volumes of 1–3 mL (72.90% vs. 73.58%, 72.74% vs. 70.39%, 71.52% vs. 68.97%), with no significant differences between architectures. However, both formats exhibited a gradual decline in viability with increasing bioink volume, more evident in scaffolds. Post-thaw proliferation further revealed comparable growth in two-dimensional and 3D cultures at 24 h, but cells in 3D scaffolds proliferated significantly faster by 48 h and 72 h (OD: 1.68 vs. 1.52; 2.37 vs. 1.94, respectively) (Figure 11B). These results indicate that architectural configuration (fiber vs. scaffold) does not directly influence cryopreservation efficiency under standardized conditions, whereas larger construct volumes reduce survival, likely due to thermal gradients impairing uniform cooling and increasing ice crystal formation risk. Importantly, 3D hydrogel scaffolds provided a superior post-thaw microenvironment, enhancing proliferation

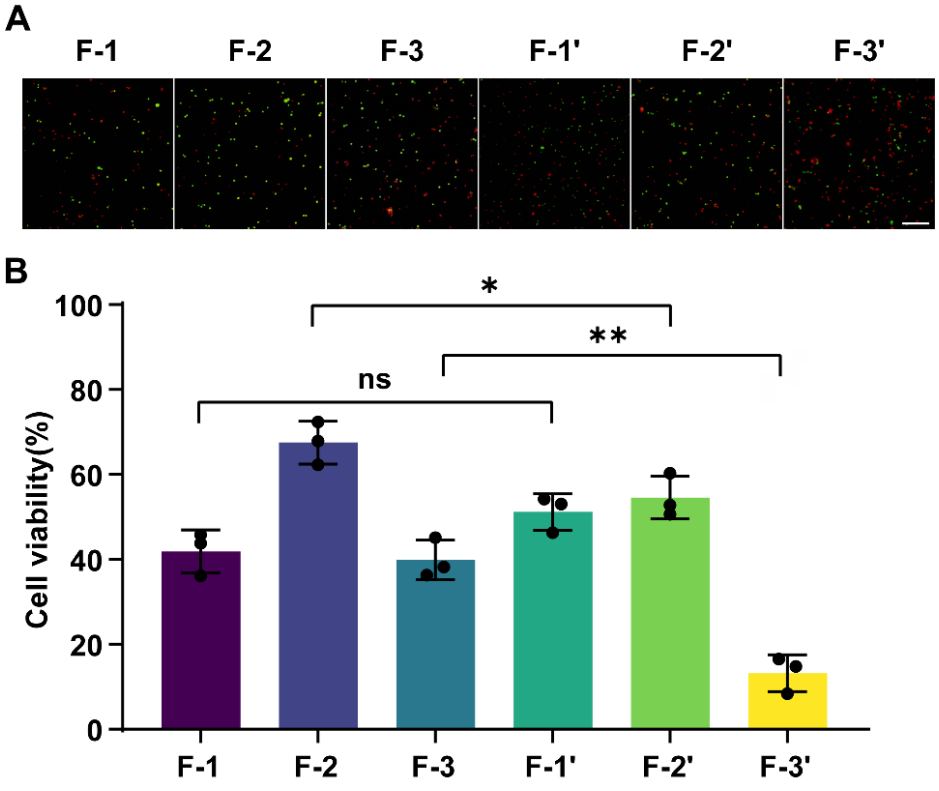


**Figure 10.** Comparison of cell cryopreservation efficiency using hydrogel scaffolds with different cooling methods. (A) Fluorescence images of live and dead cells after rewarming. Scale bar: 100 μm; magnification: 20×. (B) Cell survival rate after rewarming. Data are presented as mean ± standard deviation ($n$ = 3 independent experiments for each condition; *$p$ < 0.05, **$p$ < 0.01, ns: not significant).

in a time-dependent manner. This effect can be attributed to their biomimetic properties, which support multidirectional cell–cell and cell–matrix interactions and better recapitulate *in vivo* conditions.[44,45] Overall, these findings underscore the importance of construct scale in cryopreservation outcomes and demonstrate the advantage of 3D hydrogel scaffolds in sustaining post-thaw cell growth during *in vitro* culture.

### 3.11. Cryopreservation efficiency of C2C12 myoblasts by antifreeze hydrogels

To evaluate the universality and comparative efficacy of the antifreeze hydrogel system, we extended our assessment to C2C12 myoblasts, including a standard cryoprotectant control (10% DMSO) and hydrogel control (7% GelMA without L-proline) for rigorous benchmarking. As shown in Figure 12A,B, the post-thaw viability of C2C12 myoblasts within the L-Pro/GelMA groups exhibited a concentration-dependent decline. The 6% L-Pro + 5% GelMA group achieved the highest viability (77.37%), followed by the 7% GelMA (67.58%) and 10% GelMA (63.98%) formulations. In stark contrast, the L-Pro-free 7% GelMA control failed to provide adequate protection, resulting in a low viability (34.63%). Head-to-head control experiments using 3T3 cell-laden scaffolds under matched scaffold geometry and cell density yielded consistent results (Figure S7). Specifically, the 10% DMSO group maintained a post-thaw viability of approximately 81.57%, while the 6% L-Pro + 7% GelMA formulation achieved a comparable viability of 78.86%, with no statistically significant difference between the two groups. These findings demonstrate that the L-Pro/GelMA system provides cryoprotective efficacy similar to that of standard DMSO-based protocols, while avoiding the need for toxic organic solvents. Although the 10% DMSO positive control maintained high initial survival in both cell types, a pronounced divergence was observed

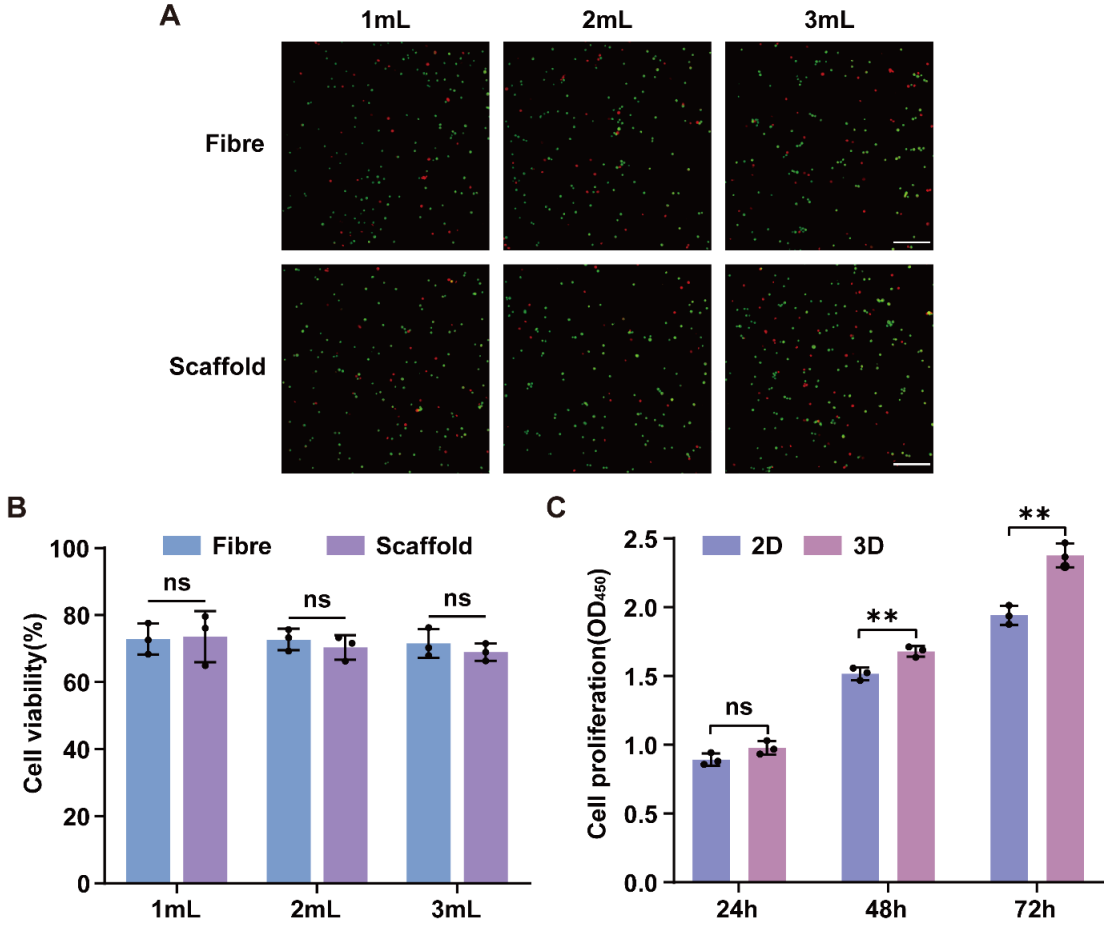


**Figure 11.** Biological performance evaluation of bioprinted constructs across different architectures, volumes, and culture modalities. (A) Fluorescence images of live and dead cells with different structures and volumes. Scale bar: 100 μm; magnification: 20×. (B) Cryopreservation efficiency of hydrogel scaffolds and fibers of different volumes. (C) Comparison of cell proliferation capacity between three-dimensional (3D) and two-dimensional (2D) cultures after rewarming. Data are presented as mean ± standard deviation ($n = 3$ independent experiments for each condition; $^{**}p < 0.01$, ns: not significant).

during the subsequent recovery phase. Proliferative kinetics over 72 h (Figure 12C,D) revealed distinct recovery profiles. Within the L-Pro groups, while the 10% GelMA formulation showed a transient lag at 24 h compared to the 5% group, all L-Pro-containing groups established robust growth by 48–72 h. Conversely, the control groups failed to sustain proliferation. The L-Pro-free group exhibited negligible growth, attributed to the critically low starting density and insufficient cell–cell synergistic interactions. Crucially, despite high initial survival, cells in the 10% DMSO group suffered from severe proliferation inhibition and eventual death over 72 h. This outcome confirms the cytotoxicity induced by residual DMSO in the absence of a post-thaw washing step, highlighting a significant limitation of conventional cryoprotectants in "washing-free" scenarios.[46,47]

Taken together, these findings indicate that the L-Pro/GelMA system provides a favorable balance between immediate post-thaw survival and long-term cytocompatibility, particularly for applications in which post-thaw washing is not feasible. While DMSO offers effective short-term cryoprotection, its practical utility may be limited by the cytotoxicity associated with residual agent; in contrast, the L-Pro/GelMA system supports high initial viability together with sustained proliferative capacity during post-thaw culture. Furthermore, the observation that lower GelMA concentrations favored C2C12 viability highlights the importance of empirical optimization to minimize biomechanical stress. Collectively, these results support the potential of this platform as a versatile, cytocompatible, and DMSO-free cryopreservation strategy for preserving cell viability and structural integrity in regenerative medicine applications.

## 4. Conclusion

This study systematically elucidated the key parameters influencing the printing and cryopreservation of cell-laden L-Pro/GelMA hydrogels, providing a framework for high-fidelity scaffold fabrication and reliable preservation of cell viability and proliferative capacity. Optimal extrusion pressures were identified for different hydrogel formulations: 25–40 kPa for 6% L-Pro + 5% GelMA, 30–50

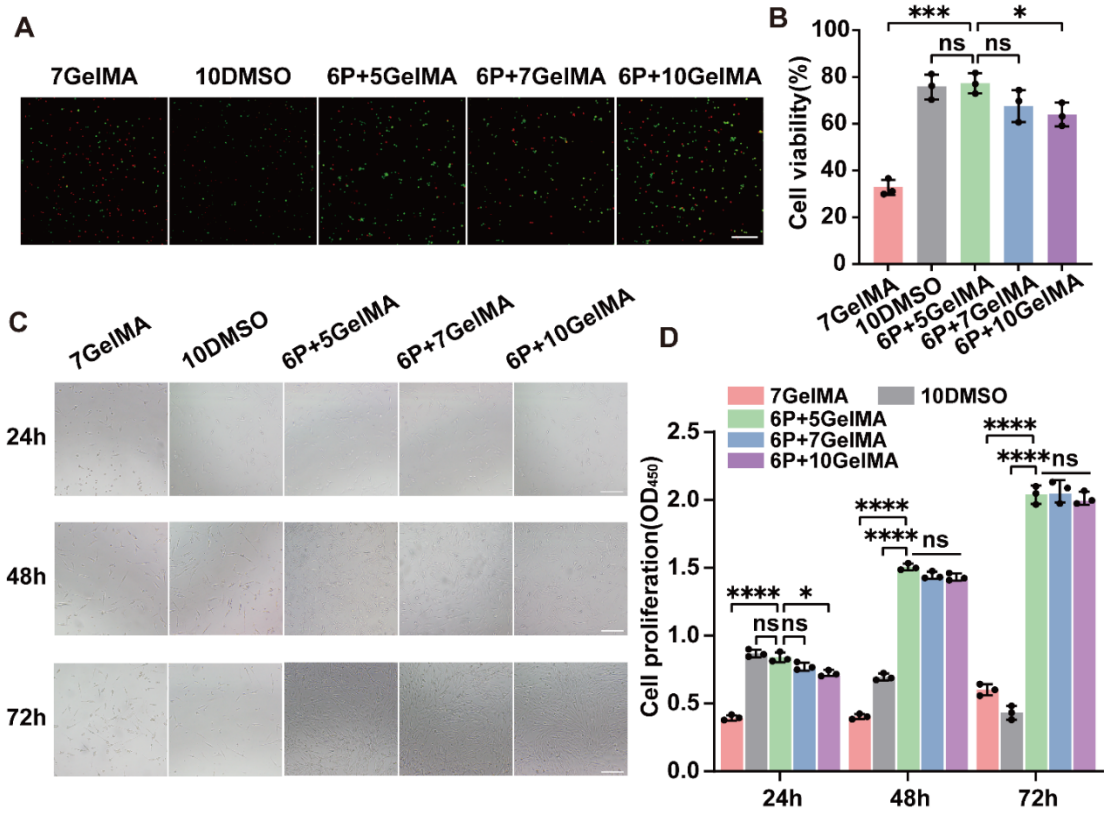


**Figure 12.** Cryopreservation effects of C2C12 myoblasts using different antifreeze hydrogels. (A) Fluorescence images of live and dead cells cryopreserved in different antifreeze hydrogel groups. Scale bar: 100 μm; magnification: 20×. (B) Cryopreservation cell survival rate. (C) Cell proliferation images after cryopreservation and thawing of different antifreeze hydrogel groups. Scale bar: 100 μm; magnification: 20×. (D) Cell proliferation rate after thawing. Data are presented as mean ± standard deviation ($n$ = 3 independent experiments for each condition; *$p$ < 0.05, ***$p$ < 0.001, ****$p$ < 0.0001, ns: not significant). Abbreviations: DMSO: Dimethyl sulfoxide; GelMA: Gelatin methacryloyl; P: L-proline.

kPa for 6% L-Pro + 7% GelMA, and 35–50 kPa for 6% L-Pro + 10% GelMA. Filament diameter increased with extrusion pressure and nozzle size but decreased with higher printing speed, reflecting the interplay between hydrogel rheology and deposition mechanics. Thermal simulations indicated maximum printable heights of 7.2–10.8 mm depending on scaffold diameter, highlighting the role of heat transfer in construct scalability.

Cytocompatibility assessments confirmed that cell viability and proliferation were preserved within defined pressure ranges, while extreme baseplate temperatures (0 °C and −5 °C) and prolonged UV exposure (>60 s) adversely affected post-printing biological activity. Cryopreservation efficiency was comparable between low-temperature and UV crosslinking, though reversible low-temperature crosslinking facilitates gentle cell recovery. F-2 cooling protocol enhanced post-thaw survival, whereas direct immersion in liquid nitrogen yielded lower viability. Notably, scaffold architecture (fiber versus multilayer) had minimal impact on preservation, but 3D hydrogel culture significantly improved post-thaw proliferation compared with conventional two-dimensional culture.

In summary, this study establishes a DMSO-free cryopreservation platform that effectively supports the preservation of 3T3 fibroblasts and C2C12 myoblasts, with lower GelMA concentrations proving beneficial for cell survival and recovery. Our findings underscore the importance of optimizing bioink formulations, printing parameters, and cooling protocols to balance scaffold fidelity, cell viability, and structural integrity. A limitation of the current study is that the post-thaw assessment focused primarily on viability and proliferation. Future studies should incorporate cell-type-specific functional assays (e.g., differentiation capacity and phenotype retention) to further validate post-thaw functionality. Overall, this platform offers a versatile strategy for cell banking and bioprinting-based tissue engineering.

## Acknowledgments

The authors wish to thank the Shanghai Cancer Energy Therapy Innovation Center and the Shanghai Bioresource Cryopreservation Technology Service Platform for providing access to experimental equipment used in this study.

## Funding

This research was supported by the Sanming Project of Medicine in Shenzhen (No. SZSM202211043).

## Conflict of interest

The authors declare no conflicts of interest.

## Author contributions

*Conceptualization:* Xin Li, Xinli Zhou
*Data curation:* Xin Li, Yukun Cao, Chenxi Liu,
*Formal analysis:* Xin Li, Jia Tan
*Funding acquisition:* Xinli Zhou, Xi Xia
*Investigation:* Xin Li, Yukun Cao
*Methodology:* Chengyuan Li
*Project administration:* Xinli Zhou, Xi Xia, Yang Yu
*Supervision:* Xinli Zhou, Yang Yu
*Writing–original draft:* Xin Li
*Writing–review & editing:* Xin Li

## Ethics approval and consent to participate

Not applicable.

## Consent for publication

Not applicable.

## Availability of data

All data analyzed in this study have been presented in the paper and in the Supplementary Materials.

## References

1. Liu K, Hu N, Yu Z, *et al.* 3D printing and bioprinting in urology. *Int J Bioprint*. 2023;9(6):0969.

   doi: 10.36922/ijb.0969

2. Pantermehl S, Emmert S, Foth A, *et al.* 3D Printing for Soft Tissue Regeneration and Applications in Medicine. *Biomedicines*. 2021;9(4):336.

   doi: 10.3390/biomedicines9040336

3. Wang H, Yang Y, Zhou X, *et al.* Rational design of mechanical bio-metamaterials for biomedical applications. *Prog Mater Sci*. 2026;156:101545.

   doi: 10.1016/j.pmatsci.2025.101545

4. Habib A, Sathish V, Mallik S, *et al.* 3D Printability of Alginate-Carboxymethyl Cellulose Hydrogel. *Materials*. 2018;11(3):454.

   doi: 10.3390/ma11030454

5. Emmermacher J, Spura D, Cziommer J, *et al.* Engineering considerations on extrusion-based bioprinting: interactions of material behavior, mechanical forces and cells in the printing needle. *Biofabrication*. 2020;12(2):025022.

   doi: 10.1088/1758-5090/ab7553

6. Ning L, Guillemot A, Zhao J, *et al.* Influence of Flow Behavior of Alginate-Cell Suspensions on Cell Viability and Proliferation. *Tissue Eng Part C Methods*. 2016;22(7):652-662.

   doi: 10.1089/ten.TEC.2016.0011

7. Wu W, Xia R, Qian G, *et al.* Mechanostructures: Rational mechanical design, fabrication, performance evaluation, and industrial application of advanced structures. *Prog Mater Sci*. 2023;131:101021.

   doi: 10.1016/j.pmatsci.2022.101021

8. Zhang YS, Haghiashtiani G, Hübscher T, *et al.* 3D extrusion bioprinting. *Nat Rev Methods Primers*. 2021;1(1):75.

   doi: 10.1038/s43586-021-00073-8

9. Ng WL, Shkolnikov V. Optimizing cell deposition for inkjet-based bioprinting. *Int J Bioprint.* 2024;10(2):2135.

   doi: 10.36922/ijb.2135

10. Law ACC, Wang R, Chung J, *et al.* Process parameter optimization for reproducible fabrication of layer porosity quality of 3D-printed tissue scaffold. *J Intell Manuf*. 2024;35(4):1825-1844.

    doi: 10.1007/s10845-023-02141-0

11. Das S, Valoor R, Ratnayake P, *et al.* Low-concentration gelatin methacryloyl hydrogel with tunable 3D extrusion printability and cytocompatibility: exploring quantitative process science and biophysical properties. *ACS Appl Bio Mater*. 2024;7(5):2809-2835.

    doi: 10.1021/acsabm.3c01194

12. Ji S, Guvendiren M. Recent Advances in Bioink Design for 3D Bioprinting of Tissues and Organs. *Front Bioeng Biotechnol*. 2017;5:23.

    doi: 10.3389/fbioe.2017.00023

13. Malda J, Visser J, Melchels FP, *et al.* 25th anniversary article: Engineering hydrogels for biofabrication. *Adv Mater*. 2013;25(36):5011-5028.

    doi: 10.1002/adma.201302042

14. Chang R, Nam J, Sun W. Effects of dispensing pressure and nozzle diameter on cell survival from solid freeform fabrication-based direct cell writing. *Tissue Eng Part A*. 2008;14(1):41-48.

    doi: 10.1089/ten.a.2007.0004

15. Correia FP, Monteiro MV, Borralho M, *et al.* Advanced Toolboxes for Cryobioprinting Human Tissue Analogs. *Adv Healthc Mater*. 2025;14(10):2405011.

    doi: 10.1002/adhm.202405011

16. Ziani K, Saenz-del-Burgo L, Pedraz J L, *et al.* Advances in Cryopreservation Strategies for 3D Biofabricated Constructs: From Hydrogels to Bioprinted Tissues. *Int J Mol Sci*. 2025;26(14):6908.

    doi: 10.3390/ijms26146908

17. Ravanbakhsh H, Luo Z, Zhang X, *et al.* Freeform Cell-Laden Cryobioprinting for Shelf-Ready Tissue Fabrication and Storage. *Matter*. 2022;5(2):573-593.

    doi: 10.1016/j.matt.2021.11.020

18. Liu M, Jiang S, Witman N, *et al.* Intrinsically cryopreservable, bacteriostatic, durable glycerohydrogel inks for 3D bioprinting. *Matter*. 2023;6(3):983-999.

    doi: 10.1016/j.matt.2022.12.013

19. Liu M, Zhang X, Guo H, *et al.* Dimethyl Sulfoxide-Free Cryopreservation of Chondrocytes Based on Zwitterionic Molecule and Polymers. *Biomacromolecules*. 2019;20(10):3980-3988.

    doi: 10.1021/acs.biomac.9b01024

20. Mahdavi SS, Abdekhodaie MJ, Kumar H, *et al.* Stereolithography 3D Bioprinting Method for Fabrication of Human Corneal Stroma Equivalent. *Ann Biomed Eng*. 2020;48(7):1955-1970.

    doi: 10.1007/s10439-020-02537-6

21. Cao K, Shen L, Guo X, *et al.* Hydrogel Microfiber Encapsulation Enhances Cryopreservation of Human Red Blood Cells with Low Concentrations of Glycerol. *Biopreserv Biobank*. 2020;18(3):228-234.

    doi: 10.1089/bio.2020.0003

22. Munesada D, Sakai D, Nakamura Y, *et al.* Investigation of the mitigation of DMSO-induced cytotoxicity by hyaluronic acid following cryopreservation of human nucleus pulposus cells. *Int J Mol Sci*. 2023;24(15):12289.

    doi: 10.3390/ijms241512289

23. Pogozhykh D, Eicke D, Gryshkov O, *et al.* Towards reduction or substitution of cytotoxic dmso in biobanking of functional bioengineered megakaryocytes. *Int J Mol Sci*. 2020;21(20):7654.

    doi: 10.3390/ijms21207654

24. Elliott GD, Wang S, Fuller BJ. Cryoprotectants: A review of the actions and applications of cryoprotective solutes that modulate cell recovery from ultra-low temperatures. *Cryobiology*. 2017;76:74-91.

    doi: 10.1016/j.cryobiol.2017.04.004

25. Troitzsch RZ, Vass H, Hossack WJ, *et al.* Molecular mechanisms of cryoprotection in aqueous proline: light scattering and molecular dynamics simulations. *J Phys Chem B*. 2008;112(14):4290-4297.

    doi: 10.1021/jp076713m

26. Szabados LSavouré A. Proline: a multifunctional amino acid. *Trends Plant Sci*. 2010;15(2):89-97.

    doi: 10.1016/j.tplants.2009.11.009

27. Kaur G, Asthir B. Proline: a key player in plant abiotic stress tolerance. *Biologia Plantarum*. 2015;59(4):609-619.

    doi: 10.1007/s10535-015-0549-3

28. Li X, Cao Y, Liu C, *et al.* l-Proline and GelMA hydrogel complex: An efficient antifreeze system for cell cryopreservation. *Cryobiology*. 2024;116:104942.

doi: 10.1016/j.cryobiol.2024.104942

29. Lee SC, Gillispie G, Prim P, *et al.* Physical and chemical factors influencing the printability of hydrogel-based extrusion bioinks. *Chem Rev*. 2020;120(19):10834-10886.

doi: 10.1021/acs.chemrev.0c00015

30. Hannah J, Zhou P. Regulation of DNA damage response pathways by the cullin-RING ubiquitin ligases. *DNA Repair*. 2009;8(4):536-543.

doi: 10.1016/j.dnarep.2009.01.011

31. Yue K, Trujillo-de Santiago G, Alvarez MM, *et al.* Synthesis, properties, and biomedical applications of gelatin methacryloyl (GelMA) hydrogels. *Biomaterials*. 2015;73:254-271.

doi: 10.1016/j.biomaterials.2015.08.045

32. Paxton N, Smolan W, Böck T, *et al.* Proposal to assess printability of bioinks for extrusion-based bioprinting and evaluation of rheological properties governing bioprintability. *Biofabrication*. 2017;9(4):044107.

doi: 10.1088/1758-5090/aa8dd8

33. Herrada-Manchón H, Fernández M A, Aguilar E. Essential guide to hydrogel rheology in extrusion 3D printing: how to measure it and why it matters? *Gels*. 2023;9(7):517.

doi: 10.3390/gels9070517

34. Zhang D, Liu J, Liu X, *et al.* Biomechanical and mechanobiological design for bioprinting functional microvasculature. *Appl Phys Rev*. 2025;12(1):011332.

doi: 10.1063/5.0227692

35. Kielbassa C, Epe B. DNA damage induced by ultraviolet and visible light and its wavelength dependence. *Methods Enzymol*. 2000;319:436-445.

doi: 10.1016/s0076-6879(00)19041-x

36. Elango JZamora-Ledezma C. Rheological, structural, and biological trade-offs in bioink design for 3d bioprinting. *Gels*. 2025;11(8):659.

doi: 10.3390/gels11080659

37. Nair K, Gandhi M, Khalil S, *et al.* Characterization of cell viability during bioprinting processes. *Biotechnol J*. 2009;4(8):1168-1177.

doi: 10.1002/biot.200900004

38. Blaeser A, Duarte Campos DF, Puster U, *et al.* Controlling Shear Stress in 3D Bioprinting is a Key Factor to Balance Printing Resolution and Stem Cell Integrity. *Adv Healthc Mater*. 2016;5(3):326-333.

doi: 10.1002/adhm.201500677

39. Xie M, Gao Q, Zhao H, *et al.* Electro-Assisted Bioprinting of Low-Concentration GelMA Microdroplets. *Small*. 2019;15(4):e1804216.

doi: 10.1002/smll.201804216

40. Adhikari J, Roy A, Das A, *et al.* Effects of Processing Parameters of 3D Bioprinting on the Cellular Activity of Bioinks. *Macromol Biosci*. 2021;21(1):e2000179.

doi: 10.1002/mabi.202000179

41. Zhang Y, O'Mahony A, He Y, *et al.* Hydrodynamic shear stress' impact on mammalian cell properties and its applications in 3D bioprinting. *Biofabrication*. 2024;16(2):022003.

doi: 10.1088/1758-5090/ad22ee

42. Chang SF, Chang CA, Lee DY, *et al.* Tumor cell cycle arrest induced by shear stress: Roles of integrins and Smad. *Proc Natl Acad Sci USA*. 2008;105(10):3927-3932.

doi: 10.1073/pnas.0712353105

43. Ahn G, Min KH, Kim C, *et al.* Precise stacking of decellularized extracellular matrix based 3D cell-laden constructs by a 3D cell printing system equipped with heating modules. *Sci Rep*. 2017;7(1):8624.

doi: 10.1038/s41598-017-09201-5

44. Cadet J, Douki T, Ravanat JL. Oxidatively generated damage to cellular DNA by UVB and UVA radiation. P*hotochem Photobiol*. 2015;91(1):140-155.

doi: 10.1111/php.12368

45. Mazur P. Cryobiology: the freezing of biological systems. *Science*. 1970;168(3934):939-949.

doi: 10.1126/science.168.3934.939

46. Yu M, Marquez-Curtis L, Elliott JAW. Cryopreservation-induced delayed injury and cell-type-specific responses during the cryopreservation of endothelial cell monolayers. *Cryobiology*. 2024;115:104857.

doi: 10.1016/j.cryobiol.2024.104857

47. Best B P. Cryoprotectant Toxicity: Facts, Issues, and Questions. *Rejuvenation Res*. 2015;18(5):422-436.

doi: 10.1089/rej.2014.1656